Early flood detection and mapping for humanitarian response

Tom De Groeve
Joint Research Center of the European Commission
tom.de-groeve@jrc.it

Patrick Riva
Joint Research Center of the European Commission
patrick.riva@ext.jrc.it

ABSTRACT

Space-based river monitoring can provide a systematic, timely and impartial way to detect floods of humanitarian concern. This paper presents a new processing method for such data, resulting in daily flood magnitude time series for any arbitrary observation point on Earth, with lag times as short as 4h. Compared with previous work, this method uses image processing techniques and reduces the time to obtain a 6 year time series for an observation site from months to minutes, with more accurate results and global coverage. This results in a daily update of major floods in the world, with an objective measure for their magnitude, useful for early humanitarian response. Because of its full coverage, the grid-based technique also allows the automatic creation of low-resolution flood maps only hours after the satellite passes, independent of cloud coverage.

Keywords

Flood detection, flood mapping, passive microwave remote sensing, early warning, humanitarian response.

INTRODUCTION

Of all natural disasters, floods are most frequent (46%) and cause most human suffering and loss (78% of population affected by natural disasters). They occur twice as much and affect about three times as many people as tropical cyclones. While earthquakes kill more people, floods affect more people (20000 affected per death compared to 150 affected per death for earthquakes) (OFDA/CRED, 2006). In general on third of humanitarian aid goes to flood related disasters. In 2008, 25 out of 43 disasters were floods, absorbing 263 million US$ or 20% of all humanitarian aid (FTS OCHA, 2009).

Nevertheless, humanitarian emergency responders have not many information sources at their disposal to learn about flood disasters. Currently, they have to rely on regional reports (such as the REDLAC Weekly Note[1]), media reports or their own global network of colleagues. One system providing a global list of flood events of potential humanitarian concern is the Global Disaster Alert and Coordination System, but its data source is the media-based catalogue compiled manually at the Dartmouth Flood Observatory. Information is scattered and not standardized, making a global compilation and relative comparison of flood events difficult. Organizations that need to prioritize humanitarian aid between ongoing disasters need to do so on an ad hoc basis. The risk then is that aid is not proportional to the size of the disaster. For instance, the floods in Bolivia in 2006, 2007 and 2008 were similar in size, fatalities, displaced persons, but funding differed significantly (see Table 1).

Table 1. Differences in funding for similar floods in Bolivia (Data sources: 1: OCHA Financial Tracking System, 2: Dartmouth Flood Observatory).

Year	Duration (days)[1]	Fatalities[1]	Displaced persons[1]	Damage (US$)[1]	Flooded area (km^2)[1]	Aid (US$)[2]
2008	138	75	240,000	200 million	866400	25.7 million
2007	112	41	62,687	90 million	801000	13.8 million
2006	83	23	100,000	35 million	955800	2.9 million

[1] A note compiled for the Risk Emergency Disaster Working Group for Latin America and the Caribbean (REDLAC) by the OCHA Regional Office.

With regional and fragmented reporting, there is also a risk to overlook flood disasters. For instance for 2008, Table 2 compares financial aid (from OCHA's Financial Tracking System; FTS OCHA, 2009) with flood severity (from the Dartmouth Flood Observatory (DFO); DFO, 2009). DFO determines flood severity based on reports of damage and fatalities and estimated recurrence interval. If no fatalities or damage was reported severity is 0; otherwise, severity is 1, 2 or 3 with respective recurrence intervals of less than 20, less than 100 and more than 100 years. In 2008, Yemen received most aid (111 million US$, of 49% of the total for the year) for relatively little casualties. India, experiencing major floods on the Brahmaputra and in the Orissa district with a combined death toll near 4000 and millions displaced, received 1% of this amount. Viet Nam, China, Brazil, Columbia and Nepal all experienced floods with more than 100 killed or more than 1 million displaced persons, but received little or no humanitarian aid.

Table 2. Comparison of humanitarian aid and flood severity. All entries of OCHA's Financial Tracking System are compared with a selected list of entries from the Dartmouth Flood Observatory catalogue.

Country	FTS OCHA aid (US$)	DFO Severity	Month in 2008	DFO Fatalities	DFO Displaced
China		3	June	176	1,600,000
Taiwan		3	July	19	
India	1,900,000	3	July	142	225,000
Mexico		3	July	1	180
China		3	July		93,000
Philippines		3	July	4	76,000
Pakistan	43,000,000	3	August	35	200,000
Iran		3	August	3	1,200
China		3	August		42,000
Viet Nam		3	August	100	
Puerto Rico		3	September	4	
Viet Nam	200,000	3	September	41	
Algeria		3	October	65	
Yemen	111,000,000	3	October	17	1,200
Brazil	400,000	3	November	117	80,000
Ecuador	7,000,000	2	January	51	265,000
Namibia	39,000,000	2	January	42	40,000
India		2	June	65	500,000
Philippines	4,000,000	2	June	1000	
India		2	July	350	70,000
Ukraine	8,000,000	2	July	40	172,000
India		2	August	74	
Thailand	5,000,000	2	August	130	4,000
Nepal		2	August	80	1,000,000
India		2	August	900	1,000,000
India		2	September	2400	
Nicaragua	50,000	2	October	9	3,000
Costa Rica	100,000	2	October	3	2,100
Honduras	8,000,000	2	October	110	320,000
Columbia		2	December	76	1,200,000
Brazil	100,000	1	January	4	15,000
Philippines	30,000	1	February	54	873,000
Kazakhstan	400,000	1	February	1	13,000
Sri Lanka	70,000	1	April	9	18,000
Kenya	200,000	1	October	3	10,000

Better, more consistent and systematic flood monitoring will allow a more systematic response to flood disasters. If this monitoring can be done in near-real time, humanitarian response can also be delivered more quickly. However, unlike for earthquakes and cyclones for which global monitoring networks exist, there is no global flood monitoring

system. Floods are difficult to monitor, because they are determined by local factors such as precipitation, slope of the terrain, drainage of the river, protection devices in place, etc. Each river must be monitored at different places along its course. Although some flood disasters occur annually, most happen unexpectedly. The 2641 floods disasters recorded in the DFO catalogue between 2000 and 2007 affected 2051 different rivers. The most flooded rivers are the Danube (22 events), the Niger (15 events), the Ganges (14 events) but 1133 rivers flooded only once in 7 years. All rivers must therefore be monitored all along their course. The number of rivers in the world is hard to determine, but even a database at scale 1:1 million (which shows only major rivers) has close to 1 million rivers[2], with a total length of 10 million km. Unlike for earthquakes were few measuring stations suffice to monitor the globe (the United States Geological survey global Seismographic network has less than 150 stations outside of America (Leith *et al.*, 2009)), an in situ global flood monitoring system would need a dense network of gauging stations along all rivers.

In situ monitoring of floods is expensive and requires advanced technical tools. The United States Streamgaging Network costs 89 million US$ per year (USGS, 1998). The most costly part is to communicate in situ data to a regional, national and international level in order to provide a global overview. Very few countries have advanced to this level. The Global Runoff Data Centre (GRDC), which collects discharge data on a global level, has data for 7300 stations, but only three countries provided data for 2008 (Australia, Norway and US; GRDC, 2009).

Alternatively, in situ measurements can be replaced by remote sensing measurements, from airplanes or satellites. Water height can be measured using radar altimetry, but not with global coverage (Bjerklie *et al.*, 2003). More important than water height for floods is the change in surface water extent. This can be extracted from aerial or satellite imagery. While the use of sensors in the visible or infrared portion of the spectrum is limited due to cloud cover, the microwave portion of the spectrum can penetrate clouds (Smith, 1997; Sippel *et al.*, 1994). However, for most remote sensing solutions, the revisit frequency (i.e. the time between two measurements in the same place) is too low for monitoring purposes or the spatial coverage is limited (Bjerklie *et al.*, 2003). For aerial imagery, the revisit time depends on flight campaigns, which are expensive. For satellite based imagery, the revisit time depends on the orbit and the image size, and at least a few sensors have daily revisit time, global coverage and provide microwave data in near-real time free of charge. These are the Advanced Microwave Scanning Radiometer - Earth Observing System (AMSR-E) instrument on board of the NASA EOS Aqua satellite (launched in 2002) and the Tropical Rainfall Monitoring Mission (TRMM).

Using AMSR-E data, De Groeve *et al.* (2006) developed a method for detecting major floods on a global basis in a systematic, timely and impartial way appropriate for humanitarian response. Brakenridge *et al* (2005) demonstrated that AMSR-E can measure river discharge changes in various climatic conditions. The methodology uses the brightness temperature at 36.5GHz H-polarization during the descending (night) orbit of AMSR-E with a footprint size of approximately 8x12km^2 and an average revisit time at 1 day. Brightness temperature is related to the physical temperature T and the emissitivity ε of an object: $T_b = \varepsilon . T$. Due to the different thermal inertia and emission properties of land and water the observed microwave radiation in general accounts for a lower brightness temperature values for water ($T_{b,water}$) and higher for land ($T_{b,land} > T_{b,water}$). Since the each observation of the satellite (or pixel) covers a relatively large area of 8x12km^2, the observed brightness temperature is mostly composed of both water and land values, in proportion to the relative area of water (w) and land ($1 - w$) in the pixel.

$$T_b = (1 - w)T_{b,land} + wT_{b,water} \qquad \text{Equation 1}$$

w = water portion of the pixel

If the physical temperature remains constant, changes in brightness temperature will be related to changes in water surface extent in the pixel. However, in spite of the great radiation dissimilarity of water and land cover, the raw brightness temperature observations cannot be used to reliably detect changes in surface water area. This is because brightness temperature (T_b) measures are influenced by other factors such as physical temperature, differences in emissitivity and atmospheric moisture. While the relative contribution of these factors cannot be measured, the authors assume them to be constant over a larger area**Error! Reference source not found.**. As shown in equation 2, the ratio between two nearby pixel values is a function of w alone. Therefore, by comparing a "wet pixel" received over a river channel of a potential inundation location ($w > 0$) with a "dry pixel" without water cover ($w = 0$) the

[2] Global Discovery database, Europa Technologies

mentioned noise factors can be reduced. The brightness temperature values of the measurement/wet signal are divided by the calibration/dry observations, referred to as M/C ratio or signal *s*.

$$T_{b,measurement} = (1-w)T_{b,land} + wT_{b,water} = T_{measurement}\left((1-w)\varepsilon_{land} + w\varepsilon_{water}\right)$$
$$T_{b,calibration} = T_{b,land} = T_{calibration}\varepsilon_{land}$$

If for nearby pixels we assume Equation 2

$$\varepsilon_{land,measurement} \approx \varepsilon_{land,calibration} \approx \varepsilon_{land}, T_{measurement} \approx T_{calibration}$$

then

$$s = \frac{M}{C} = \frac{T_{b,measurement}}{T_{b,calibration}} = \frac{T_{measurement}\left((1-w)\varepsilon_{land} + w\varepsilon_{water}\right)}{T_{calibration}\varepsilon_{land}} \approx 1 - w + w\frac{\varepsilon_{water}}{\varepsilon_{land}} = f(w)$$

When calibration pixels are chosen carefully, anomalies of the signal s can be correlated well with flood events as seen in Figure 1. Moreover, as demonstrated by Brakenridge *et al.* (2007), if gauging data is available for the site, the signal can be calibrated to staging height with accurate results.

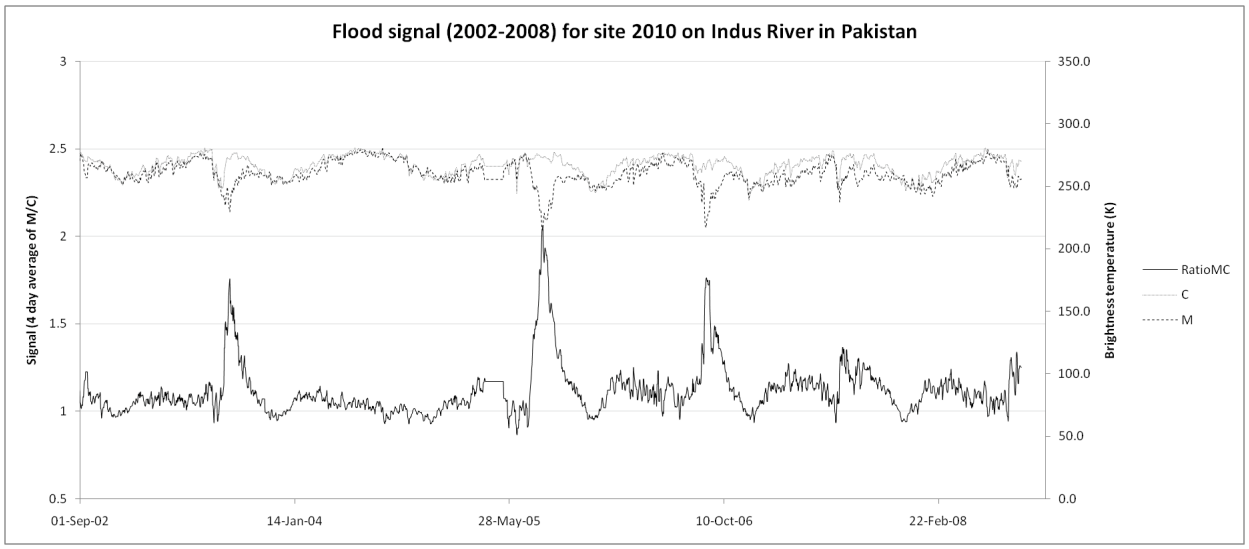

Figure 1. Example of time series of $T_{b,measurement}$ (M), $T_{b,calibration}$ (C) and the flood signal s (RatioMC) for site 2010 100km north of Hyderabad on the Indus River in Pakistan. The three peaks correspond to true flood disasters in 2003, 2005 and 2006 (from De Groeve *et al.*, 2009).

De Groeve *et al.* (2006) developed a methodology to detect floods from the M/C signal time series, going back to 2002. Since higher M/C signals generally accounts for increased water coverage, extreme events, or major floods, should represent positive anomalies in the time series of a given site. In order to detect anomalies, they first determined the reference value for normal flow, which varies for each site based on the local emissitivity properties and river geometry. This reference value was calculated as the average M/C value for the site since the launch of the satellite in 2002. They then set flood level thresholds based on the statistics of the time series. Flood magnitude was defined as the number of standard deviations (sd) from the mean (avg):

$$m = \frac{s - avg(s)}{sd(s)} \quad \text{Equation 3}$$

Kugler and De Groeve (2007) found that two problems reduced the accuracy of the system. First, calibration pixels must be carefully chosen: one must be sure that the surface water in the calibration pixel does not change. Therefore, it is labor intensive to add monitoring sites to a global flood detection system. Second, in spite of the normalization, there are still regional differences in M/C values: averages and standard deviations of time series show a lot of variation. Therefore, flood thresholds must be determined for each site individually, which is again labor intensive. The second problem can be overcome by looking at the persistence of the flood magnitudes in time and space, e.g.

by averaging flood magnitudes for neighboring sites on a river. However, this only reinforces the first problem of the manual work associated with establishing new monitoring sites.

To overcome this, a new technique was developed to use all recorded brightness temperature values in the complete coverage of the globe, abandoning the site-based flood monitoring. This technique results in more accurate flood event detection and, because of its complete spatial coverage, in early low-resolution flood mapping.

METHODOLOGY

This paper described a methodology to detect floods in a similar way as the method of De Groeve *et al.* (2006), without the need to carefully define an observation site and associated calibration pixel. First, brightness temperature observations are resampled in a fixed grid, allowing more efficient data processing and storage. Then, an alternative normalization technique is developed to obtain M/C signal values for each pixel of the global grid. Finally, the flood magnitude is determined for each pixel in the grid.

Binning brightness temperature

Instead of only retaining the observation values in a fixed radius around a predefined geographic location (a site), one can also bin all observation values in a predefined grid. We chose a grid of 4000 by 2000 pixels equally spaced in an un-projected geographic space from 180W to 180E and 90N to 90S. At the equator, each pixel corresponds to an area of around 100km^2, equivalent to the field of view of the AMSR-E instrument. Near the poles, values of each AMSR-E pixel are attributed to more than one bin, according to the projection parameters (longitudinal stretch).

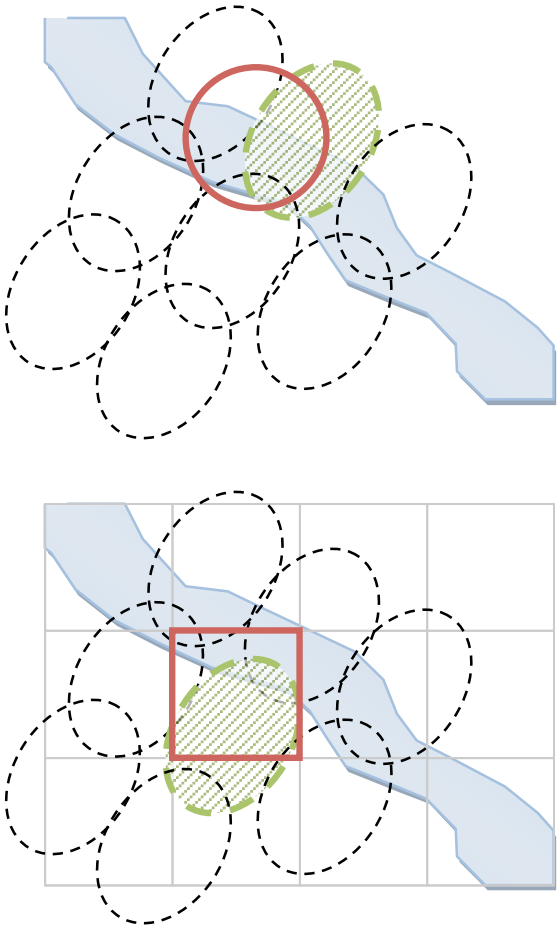

Figure 2. Site-based (left) and grid-based (right) brightness temperature determination for a target location (thick red line). Brightness temperatures of swath pixels (dotted line) are attributed to the nearest (overlapping) target (site or pixel respectively).

The coordinates of grid pixels represent the centre point of the grid pixel. The coordinates of swath pixels also represent the centre point of sensor observations. Swath pixels are assigned to the closest grid pixel, i.e. a nearest neighbor sampling approach. If more than one observation falls in the same grid pixel, their brightness temperature values are averaged. This is the case in high latitudes, where different swaths of a single day overlap.

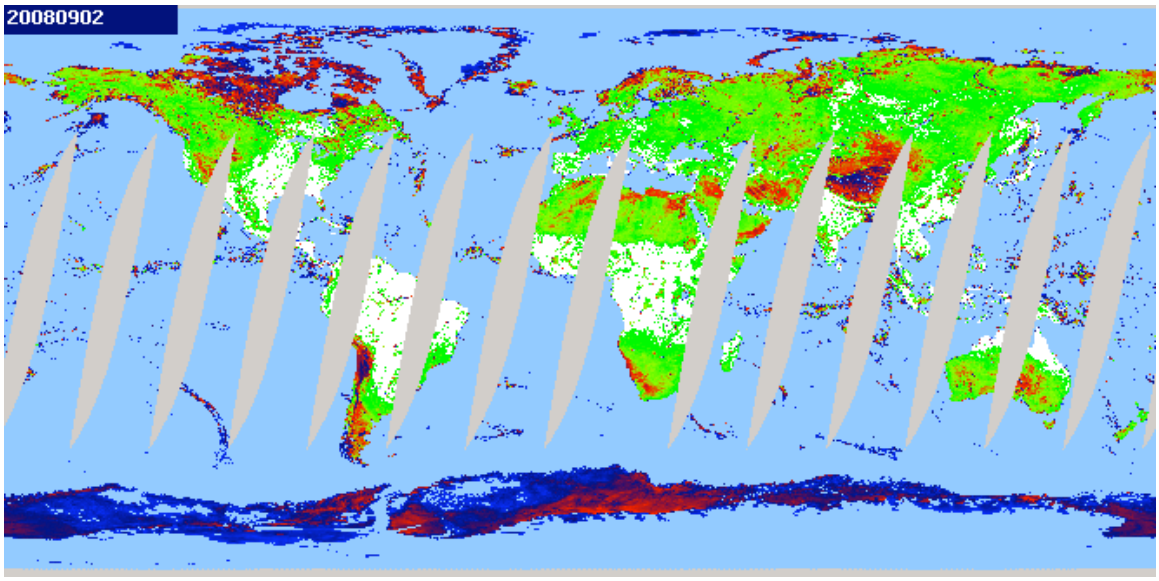

Figure 3. Example of binned swath data for 2 September 2008. Note that at lower latitudes there is no full coverage. Low brightness temperatures are shown in blue and red and are typical for polar regions, mountain ranges and rivers (e.g. Amazon basin), although also desert areas show low temperatures (at night).

A disadvantage of grid-based method compared to the site-based method is that observation sites cannot be located more precisely than about 10km. However, in both methods, observed brightness temperatures assigned to either the site or the grid pixel do not cover exactly the same area. Rather they overlap with the point of interest. Spatial variability is equally large in both methods.

Automatic selection of calibration brightness temperature

Instead of working with a well-defined (and manually selected) calibration site to obtain the calibration brightness temperature (which is the main limitation to applying the flood detection method of De Groeve *et al.* (2006) globally), we select the calibration brightness temperature as the hottest value nearby.

$$
\begin{aligned}
&T_{b,calibration} = \max_A (T_b) \\
&T_b(w) = T\left((1-w)\varepsilon_{land} + w\varepsilon_{water}\right) \\
&\varepsilon_{land} > \varepsilon_{water} \Rightarrow T_{b,\max} = T_b(0) \approx T_b(\min_A(w))
\end{aligned}
\qquad \text{Equation 3}
$$

Indeed, since surface water decreases the brightness temperature ($T_{b,land} > T_{b,water}$), the hottest site nearby must be the driest ($w = \min_A(w)$, with A the nearby area), and therefore represents the calibration temperature. This holds in most cases, except in arctic and mountain regions in freezing conditions, where $T_{b,ice} > T_{b,land}$ (Brakenridge *et al.*, 2007). However, in those cases, floods are unlikely to occur, since the river is frozen.

By looking for hot sites in a given window around a location, each pixel can be calibrated easily. In order to account for anomalously high values, we don't take the maximum brightness temperature, but rather the value representing a given percentile of all values in the window. To determine the optimum window size and percentile value, we compared times series of 4500 sites of the site-based system with times series of pixels of the grid-based system covering the location of the same 4500 sites. The latter time series were computed with varying window sizes and percentiles. In the site-based system, the average distance from manually selected calibration site to measurement

site is 62km, equivalent to 6 grid pixels, with a maximum of 450km or 45 pixels. Therefore, we chose window sizes ranging from 5 to 400km (i.e. 1 to 20 pixels half-width). With these window sizes, we selected the maximum, 97 percentile and 95 percentile temperature. Figure 4 shows that the minimum absolute difference between site-based and grid-based calibration temperatures was obtained with windows of 3 pixels half-width (i.e. distances around 30km) and using the 95th percentile value.

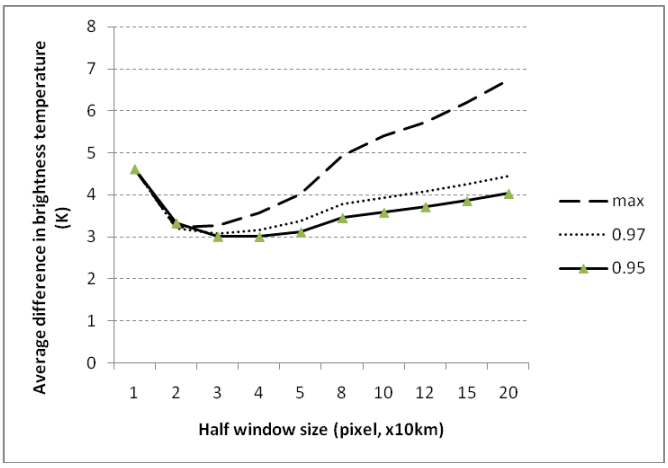

Figure 4. Optimization of calibration window size and percentile.

Grid-based flood detection

Using the daily brightness temperature grid and a way to obtain calibration values automatically, M/C signal time series similar to the site-based system can be calculated. The calibration temperature for each pixel is calculated using an image filter, selecting the 95 percentile in a window of 7 by 7 pixels around the pixel. These temperatures are stored in a new grid ("C values" of Figure 5). The M/C signal can then be obtained by computing pixel-by-pixel ratios, resulting in a calibrated image.

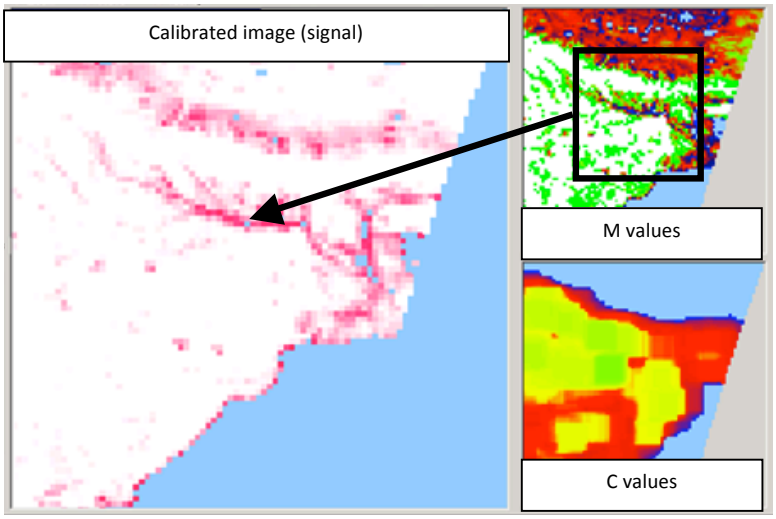

Figure 5. For each pixel in the image ("M values"), the maximum brightness temperature in a window (black box) is calculated and used a calibration value ("C values"). The calibrated image is calculated as the ratio of M and C values. The major floods of the Brahmaputra in September 2008 are clearly visible in the calibrated image, while the low brightness temperature of the Himalaya range is mostly filtered out.

Because flood magnitudes are calculated with the average and standard deviation of the time series, they can only be calculated when the complete time series is available for each pixel. After calculating calibrated images for all days

since June 2002, average values and standard deviation were calculated for each pixel. This, in turn, allowed the creation of flood magnitude images for each day since 2002.

RESULTS

Grid-based flood time series

In order to validate the grid-based methodology, we computed (M, C and M/C) time series for all GFDS sites and compared them with the site-based time series. The grid-based methodology results in time series that are comparable with the site-based time series (Figure 6). The median difference between grid-based and site-based brightness temperature is less than 0.02K, while the average is around 4K (Figure 7). Since both methods use a nearest neighbor approach, the difference results only from the slight difference in geographical location of pixel and site respectively (Figure 2).

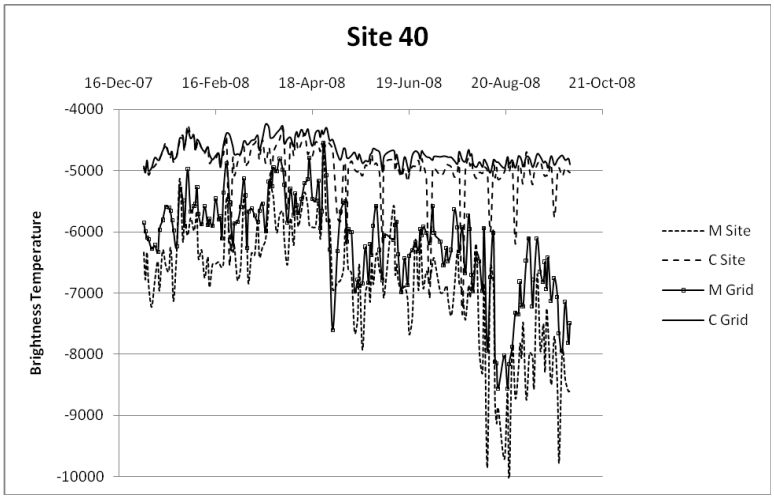

Figure 6. Comparison of grid-based and site-based brightness temperature time series (scaled to K * 100 - 32678) for site 40, near Kracheh on the Mekong River in Cambodia (12.47 North, 106 East).

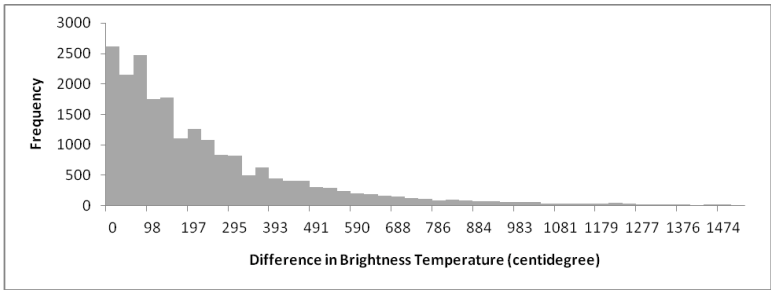

Figure 7. Histogram of difference in brightness temperature between site-based and grid-based approach (n = 21489).

With regards to the calibration temperature, Figure 4 shows that the average absolute difference in brightness temperature between site-based and grid-based calibration values is 3K. This is less than the average error introduced by the geometry of the grid (4K). This shows that the grid-based methodology to automatically select calibration temperatures cannot be distinguished from the site-based methodology where sites are selected manually.

In addition, Figure 6 shows a more consistent calibration temperature for site 41 for the grid-based method (C grid) compared to the site-based method (C site). There are no sudden drops in calibration temperature, which are most likely due to cloud coverage or other influences at the calibration pixel. Similar behavior occurs for most sites in the site-based method, and often the calibration pixel's temperature falls below the observation pixel's temperature, which is very unlikely to be true (except in cases of frozen rivers). When comparing values in the same location from the grid-based observations, this behavior disappears. Over all sites, this situation occurs for 13% of

observations in the site-based system compared to 0.5% in the grid-based system, showing the more robust way of obtaining a calibration site in the grid-based system.

Finally, also the M/C flood signal of both methods shows a good correlation (r^2 = 0.7). In particular for higher values (related to flood situations), the correlation is good (Figure 8).

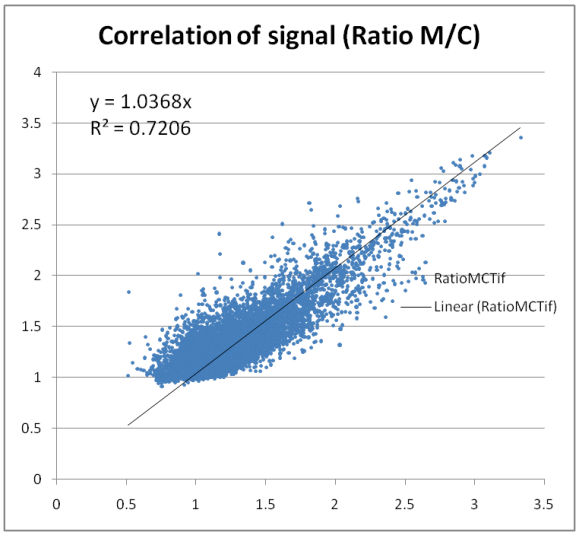

Figure 8. Correlation of M/C signal between grid-based and site-based methodology.

Figure 9 shows the time series from the grid-based system for the same example as in Figure 1.

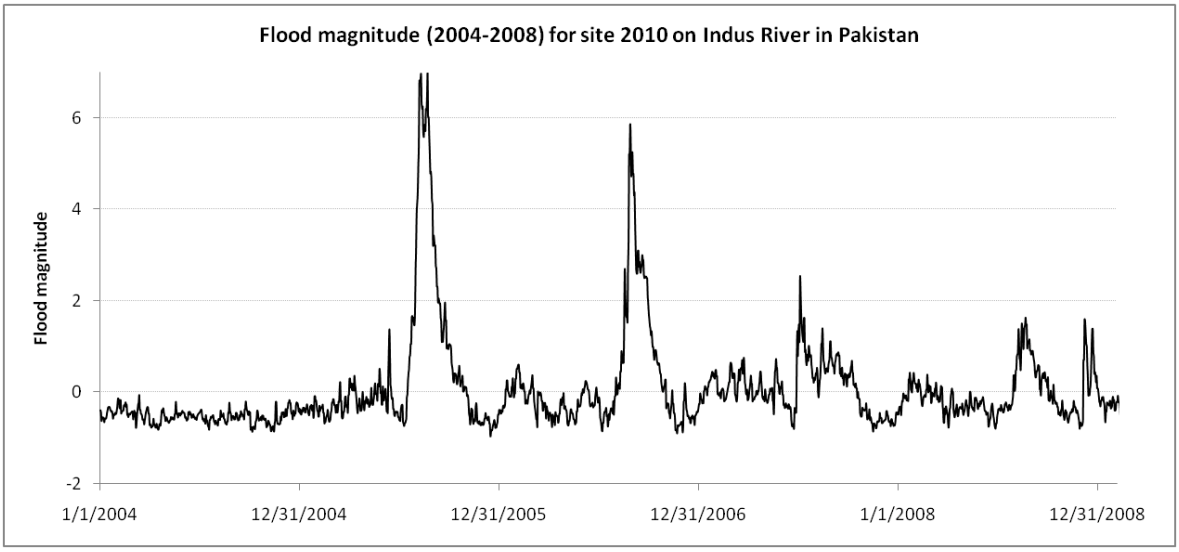

Figure 9. Flood magnitude for site 2010 near Karachi on the Indus in Pakistan. Events correspond to the major flood disasters of July 2005 (1.1 million US$ aid) and July 2006 (0.1 million US$ aid).

Early flood detection

The AMSR-E instrument has an extremely efficient data distribution mechanism making the data available for public download only hours after their acquisition. The Japanese Space Agency (JAXA) provides preliminary swath data within 1 to 4 hours after acquisition on board. This makes early flood alerting and mapping feasible.

For example, we applied this to the August / September 2008 floods in the Brahmaputra basin in India (Figure 10). Normal monsoon floods became unusual when the Kosi River (in the circle of Figure 10) breached its embankments on 18 August 2008, shifting its course nearly 100 km eastward. The flood submerged most of the Kosi alluvial fan

area, which has a dense population, causing a humanitarian disaster. The first English language media reports of this disaster appeared on 26 August, 8 days after the event.

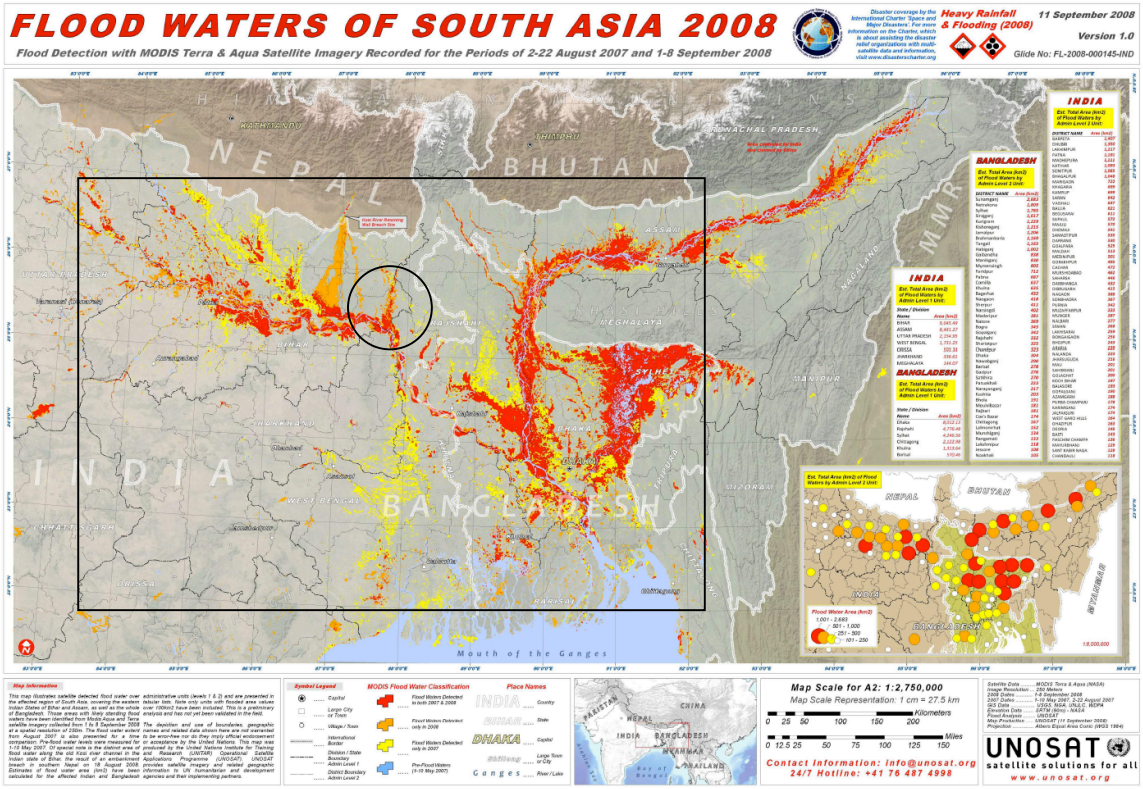

Figure 10. Overview of flood waters of South Asia in 2008 (Courtesy of UNOSAT). The black box shows the area corresponding to Figure 12. The black circle is the Kosi River, is the area of observation for Figure 11.

The number of pixels in an area around the Kosi River (composed of 34 pixels) exceeding a flood magnitude of 2 and 4 are shown in Figure 11. While the rainy period in July and early August resulted in some minor flooding in the area, a sharp rise in flooded area occurs on 19 August 2008. The area experiencing a magnitude 4 flood increases from 500km^2 on 21 August to 2500km^2 on 1 September. This information could have been available 6 days before the first international media reports.

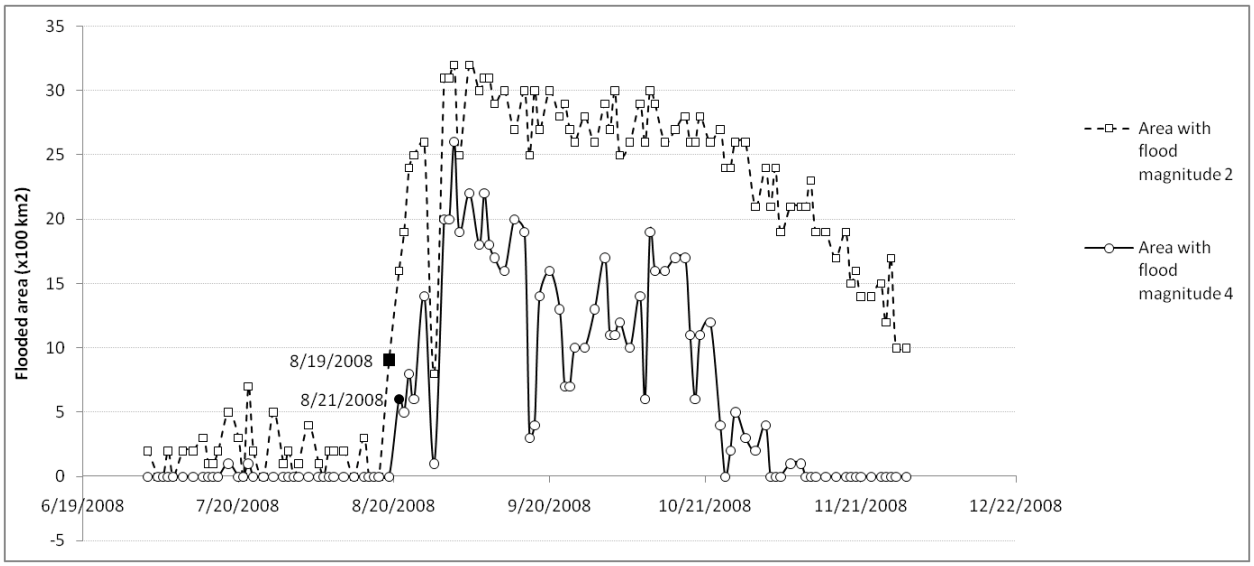

Figure 11. Flooded area, as detected in near-real time for Bihar. On 21 August 2008, 500km^2 experienced a flood of magnitude 4, which increased to a maximum of 2500km^2 on 1 September 2008.

Potential for early flood mapping

The grid-based approach results in images of M/C signals or flood magnitude. Typically, in the site-based system flood events have been defined as locations with signal anomalies over the 95% percentile, or a flood magnitude greater than 2 (De Groeve *et al.*, 2006). If the same threshold is applied, a low-resolution flood map can then be created by selecting all pixels exceeding the threshold.

While there is still noise in the images, flooded regions are clearly visible. When compared to a detailed flood map (Figure 10), the result is similar, in spite of the low resolution (10km resolution). However, this information is available within 24h of the occurrence of the flood, compared to hours after the satellite acquisition, indicating that flood magnitudes exceeding 2 are indeed corresponding to floods situations.

DISCUSSION

The new methodology for flood monitoring based on binning all brightness temperature data looks promising. In individual observation sites, the accuracy of observations, signals and flood magnitude time series is similar to the original method. However, no manual work is required to "tune" a site. We have demonstrated that the new approach to find a calibration brightness temperature works at least as good as with a well-defined and fixed calibration site, and in many cases better.

Because results can now be visualized as images, the influence of certain factors on the M/C ratio can be analyzed in detail. For instance, due to the assumption that physical temperature is constant in calibration and measurement pixel, M/C signal images show high values in areas where there is a significant temperature gradient, such as mountainous regions. Therefore, such regions must be masked out or additional calibration must be performed. Another example concerns clouds. While microwave radiation does penetrate clouds, clouds themselves also radiate energy. In fact, clouds can be clearly seen over oceans (where clouds have much higher temperatures than the ocean background, see Figure 3). Land and clouds have similar temperatures, which makes clouds difficult to filter out. Instead, clouds introduce noise in the flood signals. One way is to use information from another wavelength, particularly sensitive to clouds, and mask out areas. Another way to filter cloud noise is by temporal averaging (which is done over 4 days in the site-based system): cloud patterns change daily, while flood patterns persist usually longer. However, temporal averaging will delay flood detection since steep gradients in the flood signal are smoothed down.

With the new approach, the number of virtual gauging sites has now increased from 7500 to 8 million (one per pixel) although 2/3 are not useful because they are located in the oceans. This asks for novel processing techniques to derive flood events. In earlier work, Kugler and De Groeve (2007) have grouped information from all sites on the same river resulting in river-based flood events. Such events have a length on the river (a number of consecutive sites in flood status) and a duration in time (start and end date). A similar aggregation technique can now be applied to arbitrary areas, such as rivers, districts or even countries.

Early flood maps are another result of the new grid-based approach. While the maps are not representing the flood extent (the resolution is too low), they do show affected areas of major floods, including affected river sections and flood plains. These maps can be used to target efforts for flood extent mapping. The main advantage of the microwave-based maps is their timeliness. Maps are available in mere hours after the satellite passes, independent of cloud cover.

This new method will be implemented in the experimental Global Flood Detection System, a joint development of the Joint Research Center of the European Commission and the Dartmouth Flood Observatory (see http://www.gdacs.org/floods). This system provided experimental flood alert, meant to be included in the Global Disaster Alert and Coordination System to alert humanitarian responders in a similar way like for earthquakes and tropical cyclones.

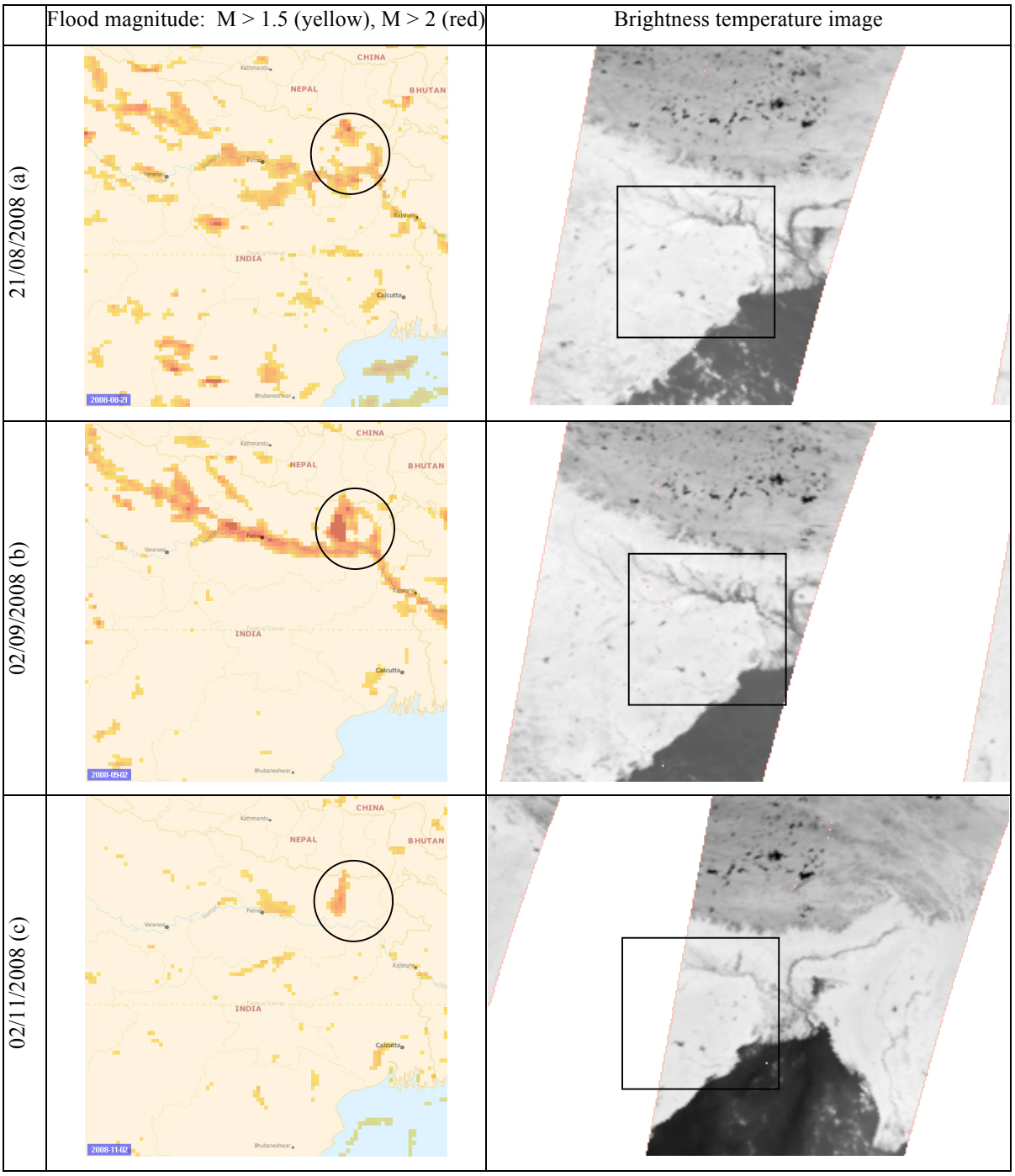

Figure 12. Flood maps of Brahmaputra, North East region of India and Bangladesh, during a major flood on 20 August (a), 2 September (b) and during normal flow (c) in November 2008. The box on the right images indicates the area of the left images. The circle in indicates a new flood channel created after the floods. In (a) the floods are in the North of the channel, filling the whole new channel in (b). An anomaly remains (c) because the new river bank does not correspond to historical data.

CONCLUSION

While floods could be accurately detected for many sites in very different parts of the world, the site-based methodology based on passive microwave remote sensing was not applicable on a global scale due to manual calibration needs for each observation site. This paper describes a grid-based flood monitoring methodology, which can bring the system one step closer to an impartial, systematic and timely flood detection system. The new methodology, with its automatic selection of calibration site, provides improved flood signals, both in terms of accuracy and coverage. In addition, the total coverage now allows aggregating information along rivers or in districts. This allows the system to monitor and alert for areas of interest for disaster managers, whether they are responsible for global monitoring or local monitoring of a district or part of a river basin. Finally, the new methodology results in automatic daily flood mapping products at 10km resolution, which can be used to identify areas for more detailed flood mapping.

Because of its global coverage and timeliness, the system can be compared to seismological networks which detect earthquakes soon after they occur. Earthquake relief benefits greatly for faster earthquake alerts, allowing to save lives. One can only hope that a similar system for floods will allow the same.

REFERENCES

1. Bjerklie, D. M., S. Lawrence Dingman, Charles J. Vorosmarty, Carl H. Bolster, Russell G. Congalton, Evaluating the potential for measuring river discharge from space, Journal of Hydrology, Volume 278, Issues 1-4, 25 July 2003, Pages 17-38, ISSN 0022-1694, DOI: 10.1016/S0022-1694(03)00129-X.
2. Brakenridge, G. R., Nghiem, S. V., Anderson, E., Chien, S. (2005) Space-based measurement of river runoff. Eos 86 (19), pp. 185-188.
3. Brakenridge, G. R., S. V. Nghiem, E. Anderson, and R. Mic (2007) Orbital microwave measurement of river discharge and ice status, *Water Resources Research, 43*, W04405.
4. De Groeve T., Z. Kugler, G. R. Brakenridge (2006) Near Real Time Flood Alerting for the Global Disaster Alert and Coordination System, Proceedings ISCRAM2007 (B. Van de Walle, P. Burghardt and C. Nieuwenhuis, eds.), pp. 33-39.
5. De Groeve, T., A. Annunziato, Z. Kugler and L. Vernaccini (2009) Near real-time global disaster impact analysis, in Information Systems for Emergency Management, Edited by Bartel Van de Walle, Murray Turoff, and Starr Roxanne Hiltz, in press.
6. DFO, 2009. Dartmouth Flood Observatory Global Active Archive of Large Flood Events, http://www.dartmouth.edu/~floods (last accessed 25 February 2009).
7. FTS OCHA, 2009. Financial Tracking Service of the Office for Coordination of Humanitarian Affairs, http://ocha.unog.ch/fts (last accessed 25 February 2009).
8. GRDC, 2009. Tabular Summary and Statistics of GRDC stations, alphabetically sorted by countries. grdc.bafg.de (last accessed 25 February 2009).
9. Kugler Z. and T. De Groeve (2007) The Global Flood Detection System. EUR 23303 EN, Luxembourg: Office for Official Publications of the European Communities, 45p.
10. OFDA/CRED (2006) 2005 disasters in numbers, OFDA/CRED, http://www.em-dat.net (last accessed 11/01/2009).
11. Smith, L. C., 1997. Satellite remote sensing of river inundation area, stage, and discharge: A review. Hydrol. Processes 11, 1427-1439.
12. Stippel, S.J., Hamilton, S.K., Melack, J.M., Choudhury, B.J., 1994. Determination of inundation area in the Amazon River floodplain using SMMR 37 GHz polarization difference. Remote Sensing Environment 48, 70–76.
13. USGS, 1998. A New Evaluation of the USGS Streamgaging Network. A report to Congress. http://water.usgs.gov/streamgaging/report.pdf (last accessed 25 February 2009).